JUDIT OLLÉ ROSELLÓ

Luminescence nanothermometry in the first and second biological windows with Yb, Nd:$KGd(WO_4)_2$, Nd:Gd_2O_3 and Yb, Nd:Gd_2O_3 nanoparticles

MASTER'S DEGREE FINAL PROJECT

Supervisors: Dr. Maria Cinta Pujol and Dr. Joan Josep Carvajal.

MASTER'S DEGREE IN NANOSCIENCE, MATERIALS AND PROCESSES

UNIVERSITAT ROVIRA i VIRGILI

Tarragona
2016

Luminescence nanothermometry in the first and second biological windows with Yb, Nd:$KGd(WO_4)_2$, Nd:Gd_2O_3 and Yb, Nd:Gd_2O_3 nanoparticles

Judit Ollé Roselló
Master Program in Nanoscience, Materials and Processes: Chemical Technology at the Frontier, 2015-2016
Supervisors: Dr. Maria Cinta Pujol and Dr. Joan Josep Carvajal.
Physics and Crystallography of Materials and Nanomaterials (FiCMA-FiCNA), Universitat Rovira i Virgili.
Campus Sescelades, c/ Marcel·lí Domingo, 1 Tarragona, 43007, Spain.

ABSTRACT:
Neodymium and Ytterbium codoped monoclinic $KGd(WO_4)_2$ and cubic Gd_2O_3 nanoparticles were synthesized by the modified Pechini sol–gel method and a microwave-assisted hydrothermal method. Under excitation at 808 nm, the 0.5 at. % Yb, 3 at. % Nd:$KGd(WO_4)_2$ nanoparticles and 0.5 at. % Yb, 3 at. % Nd^{3+}:Gd_2O_3 nanoparticles, exhibited strong emission bands at 900 nm and 1075 nm in the near infrared region range, corresponding to the $^4F_{3/2} \rightarrow {}^4I_{9/2}$ (Nd^{3+}) and $^4F_{3/2} \rightarrow {}^4I_{11/2}$ (Nd^{3+}) electronic transitions, and lying in the first and second biological windows, respectively, and an additional emission band at 1000 nm corresponding to the $^2F_{5/2} \rightarrow {}^2F_{7/2}$ (Yb^{3+}) transition, lying in the second biological window. These emissions show properties for thermal sensing in this range of wavelengths, with thermal sensitivities similar to those reported previously for more complex core-shell structures in which the doping ions were located in different layers. The results presented here indicate that the host chosen to host the lanthanide ions has an enormous influence on the thermal sensitivities that can be achieved for luminescence nanothermometry.

1. INTRODUCTION

The limitations of contact thermometers to work at the nanoscale have generated the need to develop non-contact thermometric techniques like thermoreflectance based techniques, optical interferometry, luminescent nanothermometry, Raman spectroscopy, etc [1].

In recent years, luminescent nanothermometers have been the subject of a very active field of investigation stimulated by nanotechnology and biomedicine [2]. This is due to the fact that luminescent nanothermometers work at the nanoscale and their luminescent properties change with temperature [3]. This fact is very important since temperature is a crucial parameter in science and it plays a very important role in the research and medical fields [4].

The determination of temperature by luminescent thermometers can be done through analyzing different luminescent parameters, such as the fluorescence lifetime, the optical emission intensity and the emission wavelength, among others [5]. In this paper we focused on the emission intensity ratio, which classically is based on measuring the changes of fluorescence intensities caused by temperature [6].

Until now, quantum dots, organic dyes, polymers, nanodiamonds and metal or lanthanide-doped nanoparticles (NPs) have been used as luminescent nanothermometers [7]. Among them, lanthanide-doped NPs have attracted more interest for their use as nanothermometers because of their characteristic features, like narrowband emissions, photo-stability, long luminescence lifetimes and lack of toxicity in biological media [1]. One of the recent tendencies in luminescent thermometry using lanthanides ions (Ln^{3+}) doped NPs is in the biomedical field, in which Ln^{3+} doping ions with emissions in the biological windows (BWs) are being used, since those are spectral regions where biological tissues present a reduced optical absorption and scattering of light [8]. These BWs are located in the near-infrared region of the electromagnetic spectrum, and two main windows can be distinguished: the first BW (I-BW) located from 650 to 950 nm and the second BW (II-BW) extending from 1000 to 1400 nm [9-10].

Current research is focused on Ln^{3+}-doped NPs that emit light in the spectral region of the II-BW for biomedical applications, due to the higher optical transparency of biological tissues in this particular spectral range, but specially for the reduced scattering of light, especially when compared to the I-BW, which allows for higher penetration depths and enhanced contrast for imaging applications [11]. For that reason, the development and the optimization of synthesis methods for novel NPs doped with Ln^{3+} working in the II-BW is of actual interest.

Nd^{+3} has been used as a doping ion for such applications because it has two radiative transitions located in the II-BW that can be used for thermometric purposes. In addition, this ion shows a high optical absorption cross section at around 800 nm [12], which allows exciting it in the I-BW, avoiding the excitation at 980 nm, a radiation that is absorbed by the water present in the biological tissues heating them. Yb^{3+} is used together with Nd^{3+} because of the efficient energy transfer between these two ions [12]. Furthermore, Yb^{3+} incorporates a new emission to the system in the spectral range of the BWs, which increases the number of combinations that can be used to calculate the intensity ratio from which determining the temperature [13].

In this study, we developed new luminescent nanothermometers (Ln^{3+}-doped NPs) following the ideas previously introduced in other studies, in which the use of NPs co-doped with $Nd^{+3}$and Yb^{3+} has been analyzed using $LiLaNdP_2O_{12}$ as host studied in the temperature range from 373 to 973 K with a maximum sensitivity of 0.40 % K^{-1} [13] and LaF_3 core-shell structures in which Yb^{3+} and Nd^{3+} ions can be encountered in different layers in the temperature range from 310 to 323 K with a maximum sensitivity of 0.44 % K^{-1} [14]. The novelty of our work lies in exploring others host materials to improve the thermal sensitivity of these luminescent nanothermometers. We have selected $KGd(WO_4)_2$ and Gd_2O_3 as host materials. $KGd(WO_4)_2$ NPs doped with Nd^{3+} have been used as a luminescent

nanothermometer in a previous study with good thermal sensitivity, especially in the II-BW, achieving a high penetration depth of up to 1 cm in chicken brest [15], therefore, we decided to explore if by codoping with Yb^{3+} we can still improve these results. $KGd(WO_4)_2$ (hereafter KGW), crystallizes in the monoclinic system with *C2/c* spatial group and when it is doped with Ln^{3+} ions [16], they replace Gd^{3+} in the structure [17]. This host material has a high chemical and thermal stability [18 – 19]. From another side, Gd_2O_3 NPs doped with Nd^{3+} have also been reported as luminescent nanothermometers [16], therefore, we also wanted to explore if by co-doping with Yb^{3+} we can improve these results. Finally, the comparison between the performances of these two hosts might allow getting some ideas on how the proper election of the host is a critical parameter to obtain outstanding luminescence thermometry performance. Gd_2O_3 in its cubic crystalline phase with *Ia*3 spatial group, it has also good chemical durability, thermal stability, relatively low phonon energies and can be easily doped with Ln^{3+} ions [20]. The Ln^{3+}ions replace also Gd^{3+} in the Gd_2O_3 host, in specific crystallographic positions with symmetry C_2 and C_{3i}, but the position C_3i is not spectroscopically active [21].

In this work, we optimized the doping concentrations of Yb^{3+} and Nd^{3+} in these two hosts, and analyzed their spectroscopic properties and their thermometric response in the I- and II-BWs.

2. EXPERIMENTAL TECHNIQUES

2.1 Synthesis of nanoparticles by the modified Pechini method

The modified Pechini method is a sol-gel technique used, to synthesize nanoscale materials in aqueous environment and at low temperatures. It has been already demonstrated that this method is very convenient for the synthesis of rare earth oxide nanoparticles, RE_2O_3 (RE = La, Sc, Y and Ln, lanthanides) and also for KGW [22 – 23]. The original Pechini method uses citric acid as a chelating agent (CA), but the modified Pechini method replaces citric acid by ethylenediaminetetraacetic acid (EDTA), which has a higher chelating power.

Then, EDTA react with EG to form a homogeneous sol through an esterification reaction. The methodology is reproduced based on previous works of the group where the synthesis parameters were optimized [15 – 22 – 23].

2.1.1 Synthesis of x at. % Yb, 3 at. % Nd: KGW NPs (x=0.5 to 5)

Powders of Gd_2O_3, Yb_2O_3, Nd_2O_3 (Aldrich, 99.9%) and K_2CO_3 (Alfa Aesar, 99.0%) were dissolved with the minimum volume of concentrated HNO_3 (Labkem, 65%) to synthesize x at. % Yb, 3 at. % Nd: $KGd(WO_4)_2$ NPs (x=0.5 to 5). This solution was maintained at 373 K to evaporate the excess of HNO_3 to form the metal nitrates. Then, a mixture of $(NH_4)_2WO_4$ (Aldrich, 99.99%) and EDTA (Alfa Aesar, 99.0%) dissolved in 40 ml of distilled water during 30 min at room temperature, with an EDTA molar ratio 1:1 to respect the metals dissolved in nitric acid, were added to the previously obtained dry nitrates. This solution was kept for 2 h at 323 K to favor the complexation reaction.

Next, polyethyleneglycol (Aldrich, molecular weight 400) was added to the solution at a molar ratio C_{EDTA}:C_{PEG} = 1:2, and it was mixed at the same temperature for 30 min to facilitate the esterification reaction. Then, we performed a pre-calcination step at 603 K during 3 h to start decomposing the organic resin. Finally, the precursor powder was calcined at 1277 K for 8 min and then cooled down to room temperature [15].

2.1.2 Synthesis of x at. % Nd:Gd_2O_3 NPs (x=0.5 to 5) and y at. % Yb, 3 at. % Nd:Gd_2O_3 NPs (y=0.5 to 5)

Powders of Gd_2O_3 and Nd_2O_3 were dissolved with the minimum volume of concentrated HNO_3 to synthesize 0.5 to 5 at. % Nd:Gd_2O_3 NPs. This solution was maintained at 373 K to evaporate the excess of HNO_3 to form the nitrates. Separately, EDTA was dissolved with 40 ml of distilled water during 30 min at room temperature in a molar ratio 1:1 to respect the metals dissolved in nitric acid, and this solution was added to the previously obtained dry nitrates. This solution was kept for 2 h at 323 K to favor the complexation reaction.

Next, polyethyleneglycol was added at the solution at a molar ratio C_{EDTA}:C_{PEG} = 1:2 and it was mixed at the same temperature for 30 min to facilitate the esterification reaction. Then, there was a pre-calcination step at 603 K during 1 h to start decomposing the organic gel. Finally, the precursor powder was calcined at 1073 K during 2 hours and then cooled down to room temperature. For the synthesis of the y at. % Yb, 3 at. % Nd:Gd_2O_3 NPs (y=0.5 to 5), the methodology was the same, but in this synthesis Yb_2O_3 (Aldrich, 99.9%) was added with the desired proportion to the other oxides at the beginning of the process.

2.2 Synthesis of nanoparticles by a microwave-assisted hydrothermal method

Hydrothermal synthesis techniques have raised interest of scientists and technologists from different disciplines due to the fact that are effective techniques to synthesize inorganic NPs allowing to control their morphology and size. These methods take advantage of the solubility of the inorganic substances in water at high temperature and pressure, generating after the crystallization of the dissolved material. The synthesis of 1 at. % Yb, 3 at. % Nd: KGW NPs have been done for the first time in this work following the methodology reported in the literature, taking as reference previous works based on materials such as $NaGd(WO_4)_2$ and $NaY(WO_4)_2$ [24 – 25].

2.2.1 Synthesis of 1 at. % Yb, 3 at. % Nd: KGW NPs

1 at. % Yb, 3 at. % Nd: KGW NPs were synthesized using a microwave-assisted hydrothermal method. Gd_2O_3, Yb_2O_3 and Nd_2O_3 were dissolved with the minimum volume of concentrated HNO_3. The solution was maintained at 373 K to evaporate the excess of HNO_3 and form the nitrates.

2 mmol tripotassium citrate ($C_6H_5K_3O_7$) was dissolved into 20 ml of distilled water while stirring for 20 min. $C_6H_5K_3O_7$

was used as a source of potassium. Then, 5 ml of solution containing 2 mmol of nitrates was added into the above solution, forming a white colloidal precipitate, while stirring for 15 min. 5 ml of solution containing 4 mmol $(NH_4)_2WO_4$ was added to maintain the pH in the range 8-9. The mixed solution was transferred to a Teflon vessel and was introduced into a Microwave Synthesizer MA133-004 Ethos One at 50 bar, with a power of 400 W, and the solution was irradiated from 1 to 3 h at 453 K. At the end of the reaction the vessel was cooled down to room temperature.

The precipitate was separated by centrifugation and washed with distilled water and anhydrous ethanol. Then, it was dried in a sand bath at 363 K for 1 day. Finally, the luminescent nanoparticles were obtained by calcination of the precursor powders at 1030 K for 1 h.

2.3 Characterization techniques

2.3.1 X-ray powder diffraction (XRPD)

X-ray powder diffraction was used to identify the crystalline phase of the products obtained. The equipment used in this study for the XRPD analysis is a diffractometer Bruker D8-Discover-AX. It is equipped with a Göbel mirror to produce a beam collimated incident X-ray, a θ-θ goniometer and a platform for mobile displays. For the analysis we used CuK_α radiation (λ = 1.54247 Å).

The identification of the crystalline phases was done by comparison of the recorded XRPD patterns with the reference patterns of the JCPDS database using the Diffracplus Evaluation software.

With the data obtained by XRPD and using *Scherrer* equation [see Equation 1], we estimated the average crystallite size, D [26 – 27].

$$\boldsymbol{D = \frac{k* \lambda}{\beta * \cos \theta_B}} \quad (1)$$

where k is a constant (0.9); λ is the wavelength of the radiation used; β is the full width at half maximum (FWHM) of the diffraction peak analyzed; and θ_B is the position of the Bragg peak.

2.3.2 Transmission electron microscopy (TEM)

Transmission electron microscopy is a technique with a high spatial resolution used to visualize nanoparticles and study their size and shape, as well as the degree of homogeneity of a sample. The device used in this study is a JEOL 1011 TEM.

2.3.3. Photoluminescence.

The photoluminescence of our NPs was measured using a laser emitting at 808 nm with a power of 1 W as excitation source, coupled to an optical fiber and a collimator lens that focuses the light onto an integrating sphere. The sample was introduced in the sample holder of the integrating sphere, located at 180 degrees of the pumping source and at 90 degrees of the detector. The luminescence generated by the NPs was collected by an optical fiber and was analyzed with a Yokogawa AQ6373 optical spectrum analyzer (OSA).

To determine the variation of the luminescence properties of the nanoparticles with temperature, a heating stage (Linkam THMS 600) was used. The nanoparticles were excited using a diode laser with emission at 808nm that was focused on the sample using a microscope objective. Then, the emission was collected by the same microscope objective, and after passing a dichroic filter to eliminate the excitation wavelength, the spectra were recorded by the Yokogawa AQ6373 OSA [7].

3. RESULTS AND DISCUSSION

3.1 Synthesis of the samples

Table 1 shows the different samples synthesized in this work. Using the modified Pechini method, the molar Yb^{3+} concentrations in KGW NPs were changed from 0.5 at 5, while fixing the concentration of Nd^{3+} at 3 at. %. The concentration of Nd^{3+} was optimized in a previous work [15], to achieve the maximum thermal sensitivity for luminescence thermometry purposes. In the case of Gd_2O_3, similar doping concentrations have been selected.

Table 1: Synthesized samples with their doping concentrations and crystallite sizes obtained. KGW* are NPs synthesized by the microwave-assisted hydrothermal method.

Exp.	at. % Nd^{3+}	at. % Yb^{3+}	Host	NP size [nm]
1	3	0.5	KGW	58
2	3	1	KGW	57
3	3	3	KGW	60
4	3	5	KGW	53
5	3	1	KGW*	47
6	3	1	KGW*	44
7	0.5	-	Gd_2O_3	30
8	0.75	-	Gd_2O_3	30
9	1.5	-	Gd_2O_3	30
10	2.5	-	Gd_2O_3	30
11	3	-	Gd_2O_3	31
12	3.75	-	Gd_2O_3	29
13	5	-	Gd_2O_3	30
14	3	0.5	Gd_2O_3	22
15	3	1	Gd_2O_3	23
16	3	3	Gd_2O_3	23
17	3	5	Gd_2O_3	21

The synthesized NPs were structurally characterized by XRPD. Figure 1 shows the diffraction patterns obtained for Yb,Nd:KGW and Yb,Nd:Gd_2O_3 NPs. For the Yb,Nd:KGW NPs, all the diffraction peaks observed in the experimental pattern could be indexed according to the reference JCPDS 89-8489pattern, while those of the Yb,Nd:Gd_2O_3 NPs could be indexed according to the JCPDS 12-0797 reference pattern, confirming that no other secondary crystalline products were generated in the reaction process.

Finally, Figure 1 (d) shows the experimental pattern corresponding to the Yb,Nd:KGW NPs synthesized by the microwave-assisted hydrothermal method. Again, most of the diffraction peaks observed coincide with the JCPDS 89-8489 reference pattern (see Figure 1 (e)), but there are some additional peaks, marked with (*) in the figure, which do not belong to the monoclinic phase, indicating

the presence of an additional crystalline phase that could not be identified.

Also, XRPD data were used to determine the crystallite size of the NPs obtained by the *Scherrer* equation. We used the data corresponding to the (220), (-222) and (040) diffraction peaks of the diffraction pattern of Yb,Nd:KGW NPs, determining an average crystallite size of 57 nm for the NPs synthesized by the Pechini method and 45 nm for the NPs synthesized by the microwave-assisted hydrothermal method [see Table 1] .

In the case of Gd_2O_3 NPs, we used the data corresponding to the (222), (400) and (440) diffraction peaks of the diffraction pattern, determining a mean crystallite size of 30 nm for the Nd:Gd_2O_3 NPs and 23 nm for the Yb,Nd:Gd_2O_3 NPs (see Table 1).

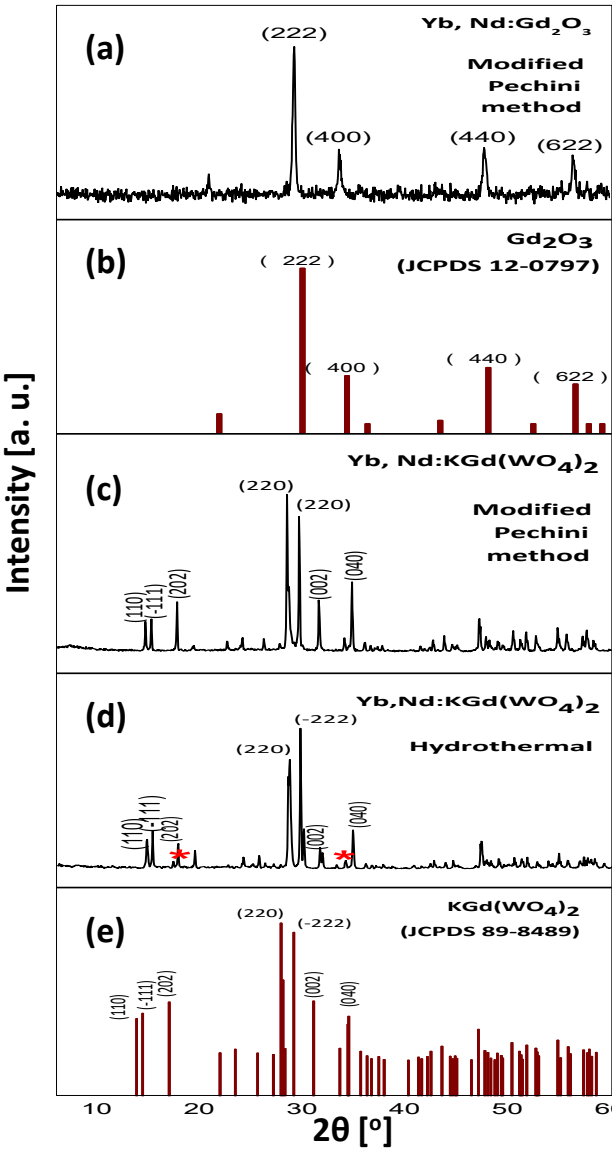

Figure 1: X-ray powder diffraction patterns of Yb and Nd co-doped Gd_2O_3 and $KGd(WO_4)_2$ NPs synthesized in this work. The reference JCPDS 12-0797 and 89-8489 patterns corresponding to cubic Gd_2O_3 (*Ia3*) and monoclinic KGW (*C2/c*), respectively, have been included for comparison.

TEM images of these NPs give information about their size distribution and morphology. Figure 2 (a) shows a representative TEM image obtained for the Nd:Gd_2O_3 NPs, where it can be observed that the size of the NPs is in the range between 20 and 50 nm, which is consistent with the results obtained by XRPD.

Figure 2 (b) shows a representative TEM image of the Yb,Nd:Gd_2O_3 NPs. Apparently, the size and morphology of these NPs is very similar to those doped only with Nd^{3+}, with a little decrease in the size of the nanoparticles as pointed out by the results obtained using the *Scherrer* equation.

Figure 2 (c) shows a representative TEM image of Yb,Nd:KGd(WO$_4$)$_2$ NPs synthesized by the Pechini method, were it is observed that the size of the NPs is in the range between 50 and 100 nm, which is consistent with the results obtained using the *Scherrer* equation.

Finally, Figure 2 (d) shows a representative TEM image of Yb,Nd:KGd(WO$_4$)$_2$ NPs obtained by the microwave-assisted hydrothermal method. Apparently, the size and morphology of these NPs is very similar to those obtained by the modified Pechini method, with a little decrease in the size of the nanoparticles as pointed out by the results obtained using the *Scherrer* equation.

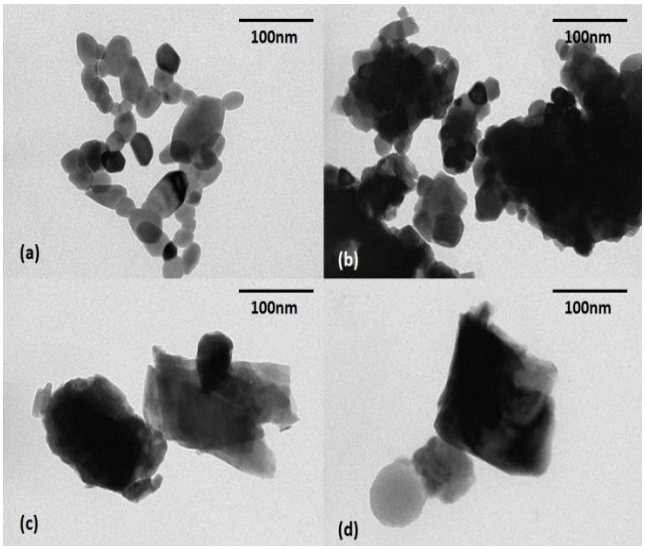

Figure 2: TEM images of: (a) 3 at. % Nd:Gd_2O_3 NPs, (b) 1 at. % Yb, 3 at. % Nd:Gd_2O_3 NPs, (c) 1 at. % Yb, 3 at. % Nd:KGd(WO$_4$)$_2$ NPs obtained by the modified Pechini method and (d) 1 at. % Yb, 3 at. % Nd:KGd(WO$_4$)$_2$ NPs obtained by the microwave-assisted hydrothermal method.

In general we can observe that the nanoparticles corresponding to sesquioxides are smaller than those of KGW, as observed previously in the literature [16-21].

3.2 Photoluminescence and nanothermometry of Yb, Nd: KGW.

3.2.1 Photoluminescence

Figure 3 (a) shows the photoluminescence under excitation at 808 nm of KGW NPs co-doped by y at. % Yb^{3+} (y = 0.5, 1, 3 and 5) and 3 at. % Nd^{3+}. They exhibited emission bands at 900 nm and 1075 nm, corresponding to the $^4F_{3/2} \rightarrow {}^4I_{9/2}$ (Nd^{3+}) and $^4F_{3/2} \rightarrow {}^4I_{11/2}$ (Nd^{3+}) electronic transitions and at 1000 nm corresponding to the $^2F_{5/2} \rightarrow {}^2F_{7/2}$ (Yb^{3+}) transition, in the NIR range. The first emission is located in the I-BW and the emissions at 1000 nm and 1075 nm are located in the II-BW.

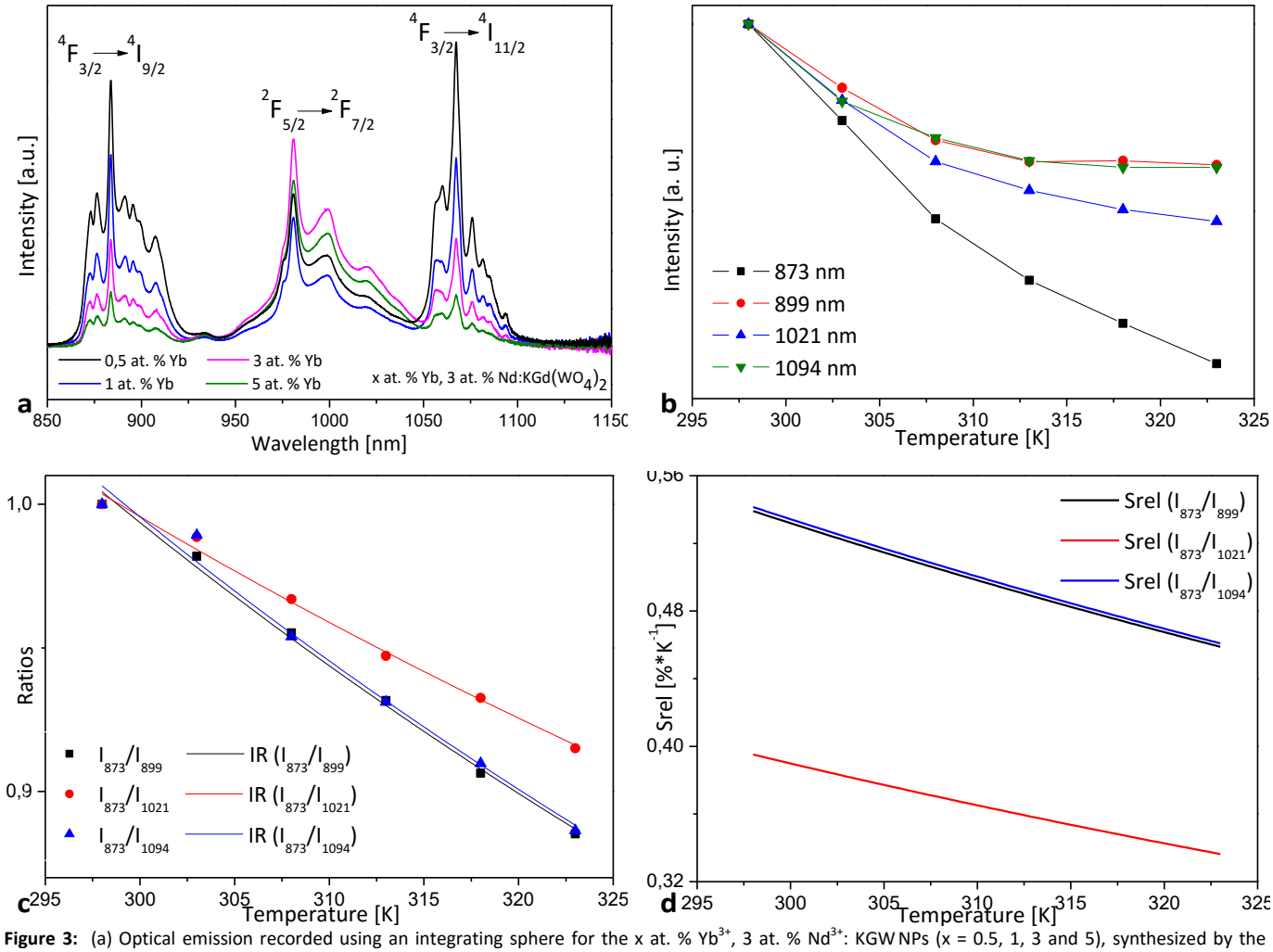

Figure 3: (a) Optical emission recorded using an integrating sphere for the x at. % Yb^{3+}, 3 at. % Nd^{3+}: KGW NPs (x = 0.5, 1, 3 and 5), synthesized by the modified Pechini method, excited at 808 nm. (b) Evolution of the emission intensity of some selected peaks which present the largest variation with temperature in 0.5 at. % Yb, 3 at. % Nd: KGW NPs. Lines are plotted only as help for visualization (c) Selected Intensity ratios (IR) in the 0.5 at. % Yb, 3 at. % Nd: KGW NPs as a function of temperature. (d) Relative thermal sensitivity (Srel) of the 0.5 at. % Yb^{3+}, 3 at. % Nd^{3+}: KGW NPs for the selected IR plotted in panel (c).

The intensity of Nd^{3+} emissions tends to decrease when the content of Yb^{3+} increased. So, this means that by exciting the Neodymium ion, the energy transfer (ET) from Neodymium to Ytterbium is more efficient as the Yb^{3+} content increases. This energy transfer is not ressonant, the difference in energy is the difference between the lowest sub-level of $^4F_{3/2}$ (Nd^{3+}) to the most energetic sub-level of $^2F_{7/2}$, and this energy difference is converted in phonons. These phonons create heat in the host, which also in turn populates by Boltzmann the highest energy sublevel of the $^2F_{5/2}$ of Yb^{3+}, enhancing the back energy transfer (BT) process from Yb^{3+} to Nd^{3+}.

This agrees with the fact that the intensity of the Ytterbium emission increases when the Yb^{3+} concentration increased from 0.5 at. % to 3 at. %, so the probability of energy transfer from Nd^{3+} to Yb^{3+} increases due to the shorter distance between Nd^{3+} and Yb^{3+}, when increasing the Yb^{3+} concentration [28]. A further increase in the Yb^{3+} content causes a diffusion of energy (diffusion transfer, DT) among ytterbium ions that causes a decrease in the intensity of the emission band arising from this ion (concentration quenching). A similar mechanism was observed previously by Marciniak et al. [14], however the energy diffusion transfer among Yb^{3+} ions at room temperature was not observed in the $LiLaNdP_2O_{12}$ with a maximum concentration of Yb^{3+} 5 at. %. These energy transfer mechanisms are plotted in Figure 4.

Thus, according to these results, the optimum concentration of dopants for enhancing Nd^{3+} emissions in KGW is 0.5 at. % Yb^{3+} and 3 at. % Nd^{3+}, while for enhancing the Yb^{3+} emission is 3 at. % Yb^{3+} and 3 at. % Nd^{3+}. The nanoparticles with these selected doping concentrations have been chosen for further characterization as nanothermometers.

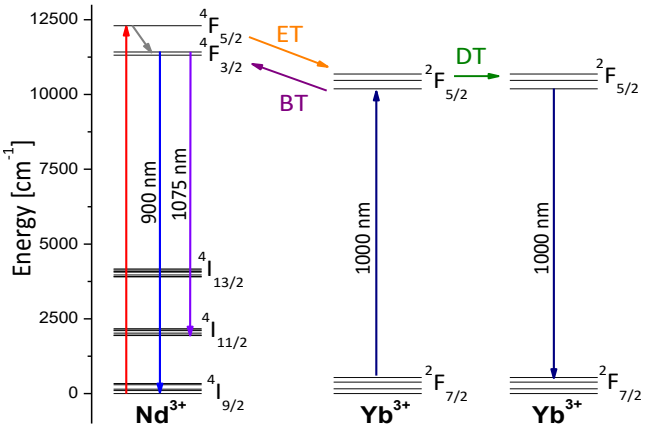

Figure 4: Energy levels of Yb^{3+} and Nd^{3+} ions and energy transfer mechanism.

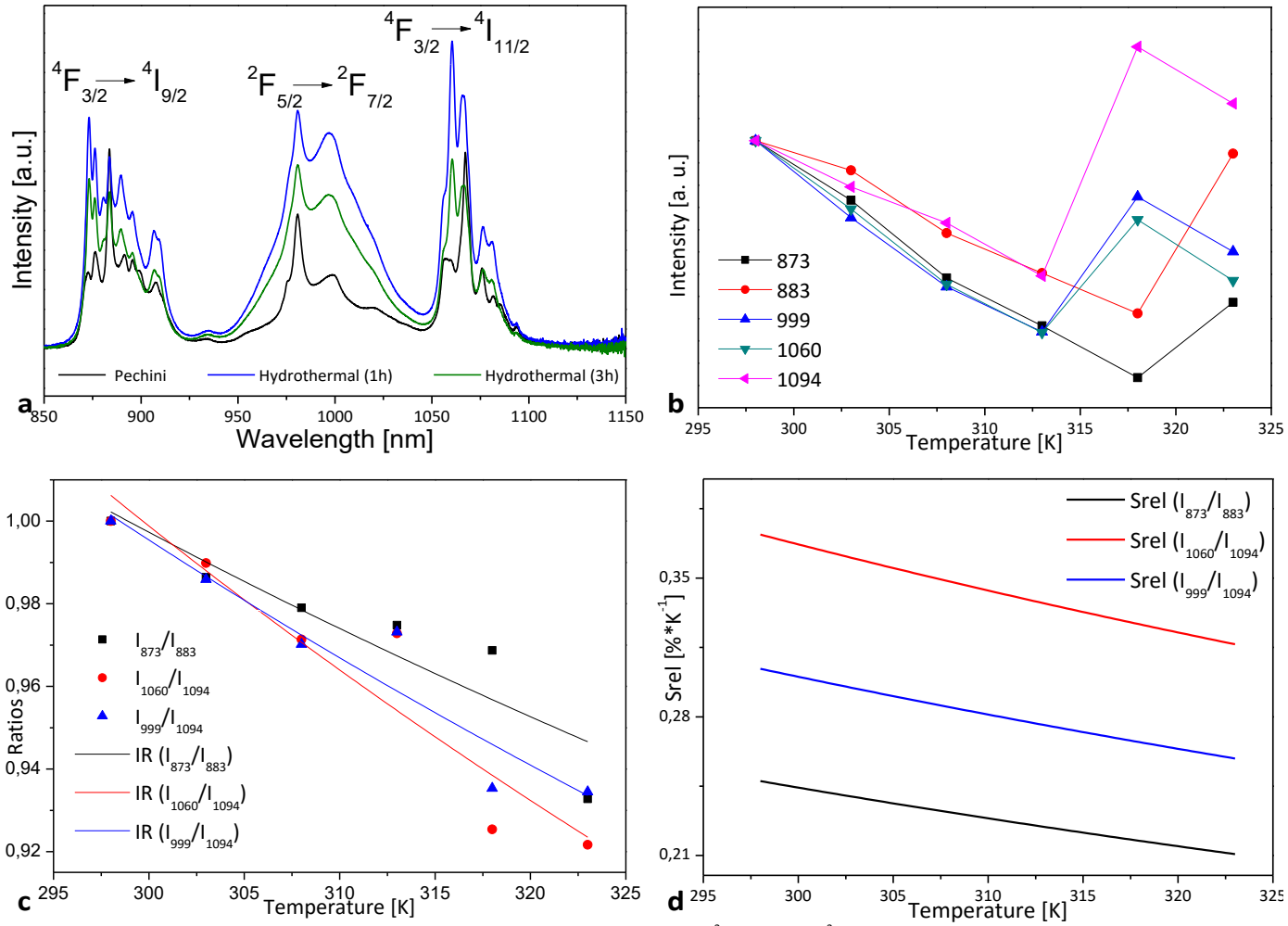

Figure 5: (a) Optical emission recorded using an integrating sphere for the 1 at. % Yb^{3+}, 3 at. % Nd^{3+}: KGW* NPs, synthesized by the microwave-assisted hydrothermal method, excited at 808 nm. (b) Evolution of the emission intensity of some selected peaks which present the largest variation with temperature in 1 at. % Yb, 3 at. % Nd: KGW* NPs. Lines are plotted only as help for visualization. (c) Intensity ratios (IR) in the 1 at. % Yb, 3 at. % Nd: KGW* NPs as a function of temperature. (d) Relative thermal sensitivity (S_{rel}) of the 1 at. % Yb^{3+}, 3 at. % Nd^{3+}: KGW* NPs for the selected IR plotted in panel (c).

Figure 5 (a) shows the emissions observed in KGW NPs co-doped by 1 at.% Yb^3 and 3 at.% Nd^{3+} prepared by the microwave-assisted hydrothermal method at different irradiation times, after excitation at 808 nm. They exhibited the same emission bands described above for the samples prepared by the modified Pechini method..

The KGW NPs synthesized by the microwave-assisted hydrothermal method exhibited a stronger intensity of emission than the KGW NPs synthesized by the modified Pechini method. Currently, we have no hypothesis for this fact, some possible reasons could be the degree of crystallinity of the samples, different molecules adsorbed on the surface of the NPs that affect to the non-radiative processes and/or different effective doping concentrations. Further studies should be performed to clarify this aspect. The sample showing the highest intensity is the one irradiated with microwaves during 1h. These are the nanoparticles we have chosen also for further characterization as nanothermometers.

3.2.2 Nanothermometry.

To know the potential use of Yb,Nd:KGW NPs synthesized by the modified Pechini method and the microwave-assisted hydrothermal method for thermal sensing, it requires to know the evolution of the intensity of the photoluminescence bands with temperature. The emission spectra obtained for those NPs were recorded at different temperatures ranging from 298 to 323K, within the physiological range.

Thermal sensing is achieved by the analysis of the changes in the emission intensity caused by temperature [29]. The intensity ratios (IR) we calculated could be empirically fitted to the following equation:.

$$IR = A * \exp\left(\frac{-B}{T}\right) \qquad (2)$$

where, A and B are constants and T is the absolute temperature.

To compare the temperature sensing capacity among nanophosphors it is necessary to know the changes in the intensity ratios calculated for a small change in temperature using the absolute sensitivity (S_{abs}), which can be calculated from the first derivative of the intensity ratio with respect to the temperature:

$$Sabs = \frac{dIR}{dT} \qquad (3)$$

To make easy the comparison the use of the relative

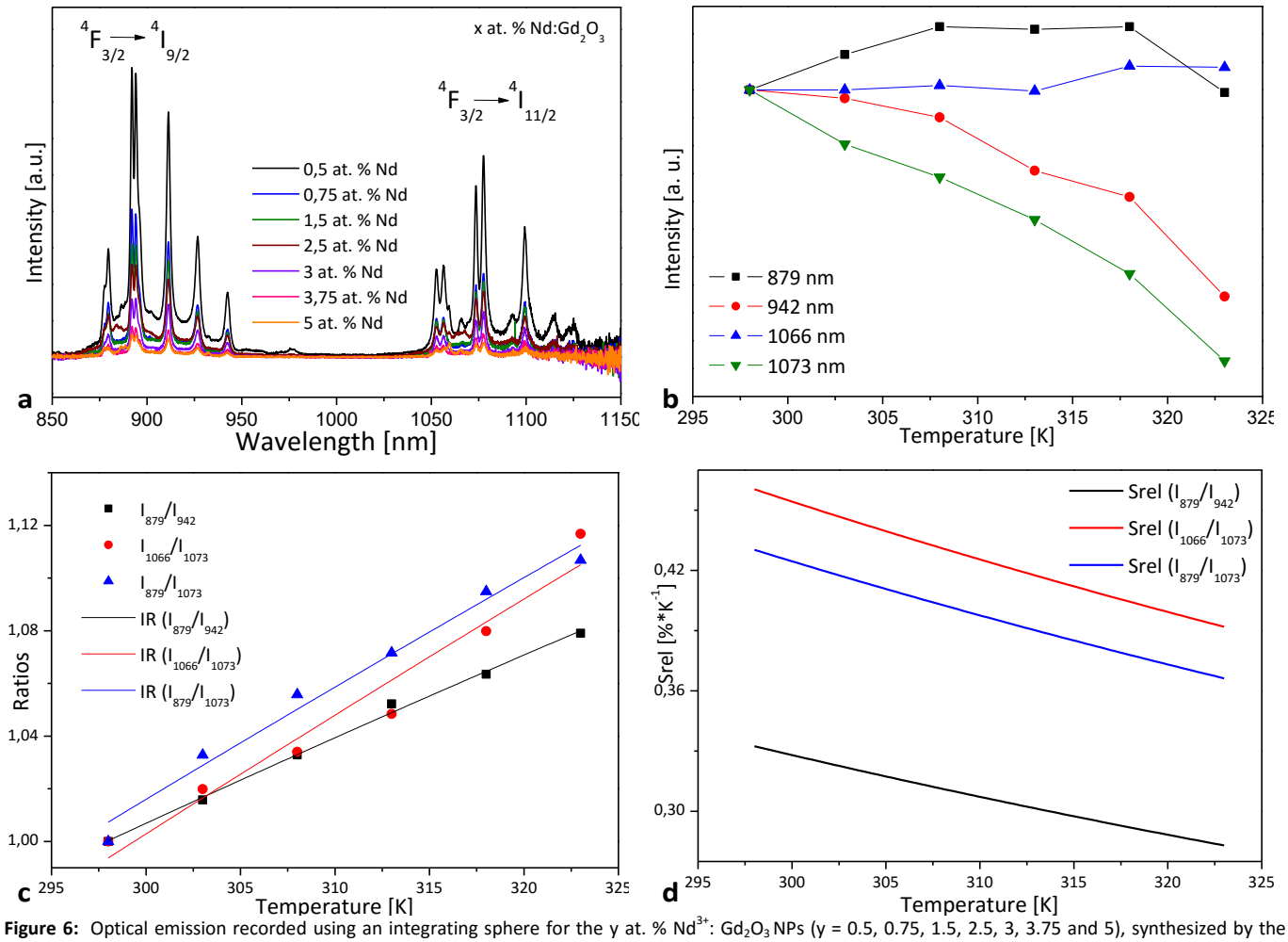

Figure 6: Optical emission recorded using an integrating sphere for the y at. % Nd^{3+}: Gd_2O_3 NPs (y = 0.5, 0.75, 1.5, 2.5, 3, 3.75 and 5), synthesized by the modified Pechini method, excited at 808 nm. (b) Evolution of the emission intensity of some selected peaks which present the largest variation with temperature in 0.5 at. % Nd: Gd_2O_3 NPs. Lines are plotted only as help for visualization. (c) Selected Intensity ratios (IR) in the 0.5 at. % Nd: Gd_2O_3 NPs as a function of temperature. (d) Relative thermal sensitivity (Srel) of the 0.5 at. % Nd^{3+}: Gd_2O_3 NPs for the selected IR plotted in panel (c)..

sensitivity has been suggested:

$$Srel = \frac{Sabs}{IR} \qquad (4)$$

Figures 3 (b) and 5 (b) show the evolution of the intensity of the peaks that were selected to calculate the IR since their intensities show a larger variation with the temperature.

In Figures 3 (c) and 5 (c) the intensity ratios with larger variations with temperature can be seen. Focuses with the ratios, in the figure 3 (c) there is the ratios of $I_{873}/_{899}$ (R=0.9942), I_{873}/I_{1021} (R=0.9916) and I_{873}/I_{1094} (R=0.9833 I) of the 0.5 at. % Yb^{3+}, 3 at. % Nd^{3+}: KGW NPs. The ratio of I_{873}/I_{899} describes the Boltzmann population from the fundamental state to the sub-level 3 ($^4F_{3/2}$ (2') $\rightarrow$ $^4I_{9/2}$ (0) / $^4F_{3/2}$ (2') $\rightarrow$ $^4I_{9/2}$ (3)). In the ratio of I_{873}/I_{1021}, there is a negative slope because of the temperature's increase, as a result, the ET is encouraged ($^4F_{3/2}$ (2') $\rightarrow$ $^4I_{9/2}$ (0) / $^4F_{5/2}$ (0') $\rightarrow$ $^2F_{7/2}$ (2)). The ratio of I_{873}/I_{1095} describes the Boltzmann population from the fundamental state to the sub-level 5 ($^4F_{3/2}$ (2') $\rightarrow$ $^4I_{9/2}$ (0) / $^4F_{3/2}$ (1') $\rightarrow$ $^4I_{11/2}$ (5)). Finally, the figure 5 (c) there is the ratios of I_{873}/I_{883} (R=0.8027), I_{1060}/I_{1094} (R=0.8686) and I_{999}/I_{1094} (R=0.8857) of the 0.5 at. % Yb^{3+}, 3 at. % Nd^{3+}: KGW NPs (microwave – assisted hydrothermal). The ratio of I_{873}/I_{883} describes the Boltzmann population from the fundamental state to the sub-level 0 ($^4F_{3/2}$ (2') $\rightarrow$ $^4I_{9/2}$ (0) / $^4F_{3/2}$ (1') $\rightarrow$ $^4I_{9/2}$ (0)). The ratio of I_{1060}/I_{1094} describes the Boltzmann population from the fundamental state to the sub-level 5 ($^4F_{3/2}$ (2') $\rightarrow$ $^4I_{11/2}$ (0) / $^4F_{3/2}$ (1') $\rightarrow$ $^4I_{11/2}$ (5)). The ratio of I_{999}/I_{1094} describes

Table 2: Information of the maximum S_{rel} of the nanoparticles created in this study and the nanoparticles of the bibliography. The * is for the samples prepared by microwave-assisted hydrothermal.

Nanoparticles	S_{rel} in the I-BW [%*K^{-1}]	S_{rel} in the II-BW [%*K^{-1}]	Temperature [K]
Yb, Nd:KGW	0.54	0.54	298 - 323
Yb, Nd:KGW*	0.25	0.37	298 - 323
Nd:KGW [15]	0.12	0.17	298 - 333
Nd:Gd_2O_3	0.33	0.46	298 - 323
Yb, Nd:Gd_2O_3	1.30	0.82	298 - 323
Nd, Yb:LiLaNdP_2O_{12} [13]	0.40	-	373 - 973
Nd, Yb:LaF_3 [14]	-	0.44	310 - 323

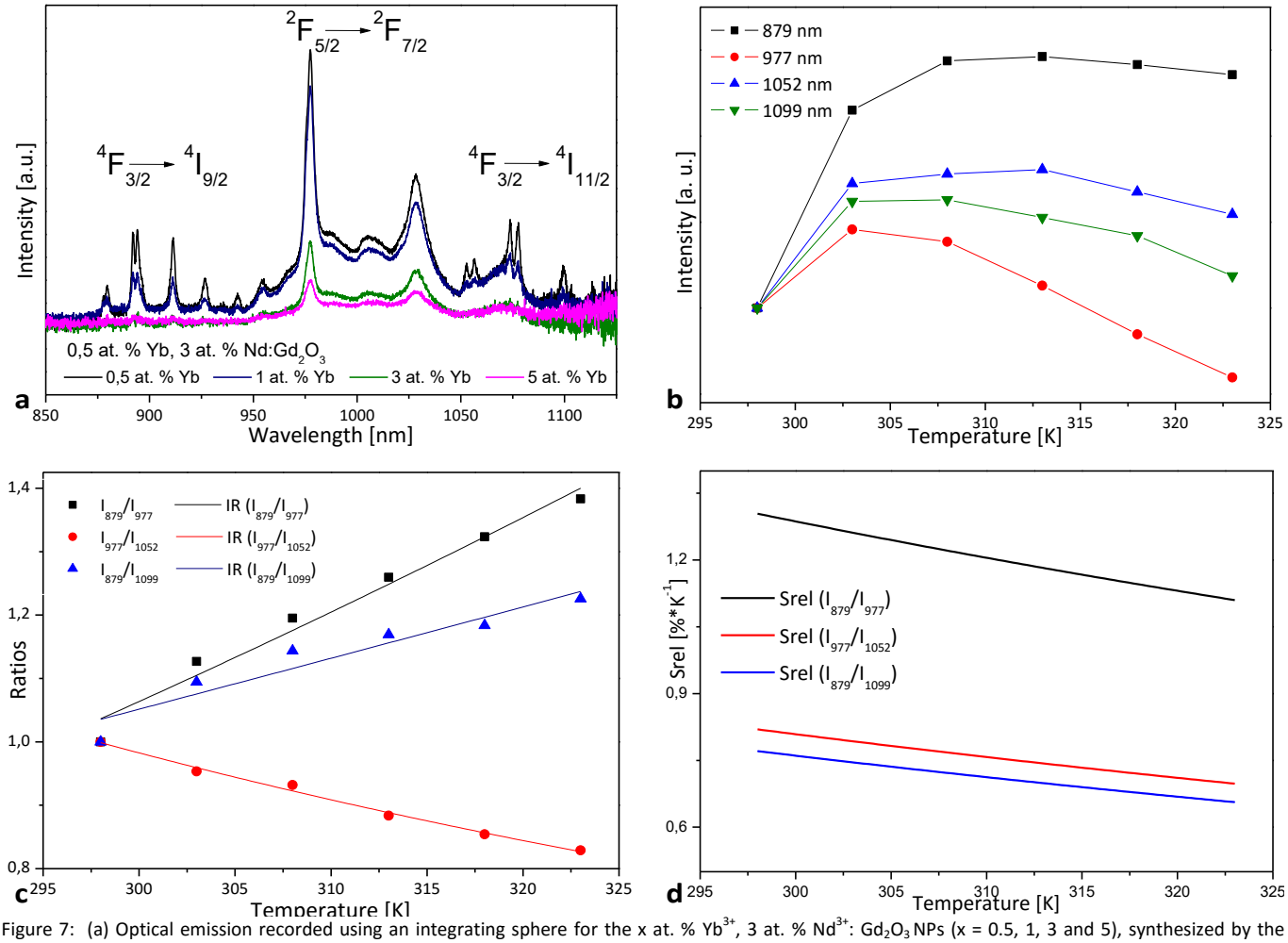

Figure 7: (a) Optical emission recorded using an integrating sphere for the x at. % Yb^{3+}, 3 at. % Nd^{3+}: Gd_2O_3 NPs (x = 0.5, 1, 3 and 5), synthesized by the modified Pechini method, excited at 808 nm. (b) Evolution of the emission intensity of some selected peaks which present the largest variation with temperature in 0.5 at. % Yb, 3 at. % Nd: Gd_2O_3 NPs. Lines are plotted only as help for visualization. (c) Selected Intensity ratios (IR) in the 0.5 at. % Yb, 3 at. % Nd: Gd_2O_3NPs as a function of temperature. (d) Relative thermal sensitivity (Srel) of the 0.5 at. % Yb^{3+}, 3 at. % Nd^{3+}: Gd_2O_3NPs for the selected IR plotted in panel (c).

the temperature's increase, as a result, the ET is encouraged ($^4F_{5/2}$ (0') $\rightarrow$ $^2F_{7/2}$ (1) / $^4F_{3/2}$ (1') $\rightarrow$ $^4I_{11/2}$ (5)).

Figures 3 (d) and 5 (d) show the relative thermal sensitivities (S_{rel}) achieved with the different IR in KGW NPs and in the table 2 can be seen the values of the maximum S_{rel} of the previous NPs and the values of the bibliography.

The maximum relative sensitivity at 300 K is 0.54 % K^{-1} belonging to the 0.5 at. % Yb, 3 at. % Nd: KGW NPs using the I_{873}/I_{899} and I_{873}/I_{1094} IRs, located in the I-BW and in the I-BW and II-BW, respectively.

If we compare these results with those of the study of Savchuk et al. [15] (0.165 % K^{-1}), a better sensitivity is obtained with the new NPs.

3.3 Photoluminescence and nanothermometry of Nd^{3+}:Gd_2O_3 and Yb^{3+}, Nd^{3+}:Gd_2O_3 NPs

3.3.1. Photoluminescence.

Figure 6 (a) shows the emission spectra recorded for Gd_2O_3 NPs doped by x at. % Nd^{3+} (x = 0.5, 0.75, 1.5, 2.5, 3.75 and 5) after excitation at 808 nm. They exhibited the same emission bands at 900 nm and 1075 nm observed before in KGW NPs. The intensity of the Nd^{3+} emissions tends to decrease when the Nd^{3+} concentration increased from 0.5 at. % to 5 at. %. A similar mechanism was observed previously in the bibliography [30]. The 0.5 at.% Nd^{3+}: Gd_2O_3 exhibited the strongest intensity of emission. A possible mechanism to observe a so severe quenching for so low concentrations might be the non-radiative cross relaxation process among Neodymium ions; which due to the short distances among the ions in this host [31].

Figure 7 (a) shows the emission spectra corresponding to Gd_2O_3 NPs codoped by 3 at.% Nd^{3+} and y at.% Yb^{3+} (y = 0.5, 1, 3 and 5) after excitation at 808 nm. Apart from the Nd^{3+} bands observed previously, the 1000 nm emission band corresponding to the $^2F_{5/2} \rightarrow {}^2F_{7/2}$ (Yb^{3+}) transition is also observed.

At first sight, it can be observed that in this host, the ytterbium emission is predominant versus the Neodymium ones; so, generally speaking in this host the energy transfer is more favored or the concentration quenching of Neodymium through the cross relaxation process is less efficient in the KGW host.

The 0.5 at.% Yb^{3+}, 3 at.% Nd^{3+}: Gd_2O_3 NPs exhibited the strongest emission, the intensity of the emission increases when the Yb^{3+} concentration decreased from 5 at. % to 0.5 at. %, so the probability of energy transfer from Nd^{3+} to Yb^{3+} increases due to the shorter distance between Nd^{3+} and Yb^{3+}, when increasing the Yb^{3+} concentration [32].

3.3.2 Nanothermometry.

To know the potential use of Nd^{3+}: Gd_2O_3 NPs and Yb^{3+}, Nd^{3+}: Gd_2O_3 NPs for thermal sensing, it requires to know the thermal response of the intensity of the luminescence bands. The emission spectra obtained for those NPs were recorded at different temperatures (from 298 to 323K) within the physiological range.

Figures 6 (b) and 7 (b) show the evolution of the intensity of the peaks that were selected to calculate the IR since their intensities show a larger variation with the temperature.

In Figures 6 (c) and 7 (c) the intensity ratios with larger variations with temperature can be seen. Focuses with the ratios, in the figure 6 (c) there is the ratios of I_{879}/I_{942} (R=0.9961), I_{1066}/I_{1073} (R=0.9457) and I_{879}/I_{1073} (R=0.9776) of the 0.5 at. % Nd^{3+}:Gd_2O_3 NPs. In this case, the slopes are positives related to the phenomenon of cross relaxation which is very important in this host. The ratio of I_{879}/I_{942} describes the Boltzmann population from the sub-level 1 to the sub-level 4 ($^4F_{3/2}$ (2') $\rightarrow$ $^4I_{9/2}$ (1) / $^4F_{3/2}$ (1') $\rightarrow$ $^4I_{9/2}$ (4)). The ratio of I_{1066}/I_{1073} describes the Boltzmann population from the fundamental state to the sub-level 1 ($^4F_{3/2} \rightarrow {}^4I_{11/2}$ / $^4F_{3/2}$ (1') $\rightarrow$ $^4I_{11/2}$ (1)). The ratio of I_{879}/I_{1073} describes the Boltzmann population from the sub-level 1 to the sub-level 2 ($^4F_{3/2}$ (2') $\rightarrow$ $^4I_{9/2}$ (1) / $^4F_{3/2}$ (1') $\rightarrow$ $^4I_{11/2}$ (2)). Finally, the figure 7 (c) there is the ratios of I_{879}/I_{977} (R=0.9664), I_{977}/I_{1052} (R=0.9907) and I_{879}/I_{1099} (R=0.8872) of the 0.5 at.% Yb^{3+}, 3at.% Nd^{3+}:Gd_2O_3 NPs. Also, in this case, the slopes are positives for the I_{879}/I_{977} and I_{879}/I_{1099}, and negative for I_{977}/I_{1052}. The ratio of I_{879}/I_{977} (positive slope) describes the diffusion between ytterbium ions ($^4F_{3/2}$ (2') $\rightarrow$ $^4I_{9/2}$ (1) / $^4F_{5/2}$ (0') $\rightarrow$ $^2F_{7/2}$ (0)). The ratio of I_{977}/I_{1052}, describes the Boltzmann population from the fundamental state to the sub-level 0 ($^4F_{5/2}$ (0') $\rightarrow$ $^2F_{7/2}$ (0) / $^4F_{3/2}$ (2') $\rightarrow$ $^4I_{11/2}$ (0)). The ratio of I_{879}/I_{1099} describes the Boltzmann population from the sub-level 1 to the sub-level 2 ($^4F_{3/2}$ (2') $\rightarrow$ $^4I_{9/2}$ (1) / $^4F_{3/2}$ (1') $\rightarrow$ $^4I_{11/2}$ (2)).

Figure 6 (d) and figure 7 (d) show the relative thermal sensitivities (S_{rel}) achieved with the different IR in Gd_2O_3 NPs and in the table 2 can be seen the values of the maximum S_{rel} of the previous NPs and the values of the bibliography.

The maximum thermal sensitivity at 300 K is 1.30% K^{-1} belonging to the 0.5 at. % Yb^{3+}, 3 at. % Nd^{3+}:Gd_2O_3 NPs using the $I_{879}/I_{977,}$ IR, located in the I-BW. However, also a high thermal sensitivity can be obtained in the II-BW, using the ratio I_{977}/I_{1052} IR, improving also the vales previously reported in the literature.

Comparing the values of relative thermal sensitivity in these two different hosts, a higher thermal sensitivity is obtained in Gd_2O_3 NPs. This implies that the host selected plays a major role in defining the luminescent thermometric properties, although at present which are the particular characteristics of the host that affects the most to these properties are not known, and further work will be required to do to evaluate them. Furthermore, in both hosts, it can be observed an increase of the relative thermal sensitivity when co-doping with Yb^{3+} when compared to Nd^{3+} monodoped samples.

4. CONCLUSIONS

In summary, we performed an investigation of the luminescence properties of Yb, Nd:KGd$(WO_4)_2$, Nd:Gd_2O_3 and Yb, Nd:Gd_2O_3 nanocrystals in relation with temperature. The thermal characterization of the luminescence properties of these nanoparticles indicates that they can be used as efficient luminescent nanothermometers in the I-BW and II-BW. A maximum thermal relative sensitivity of 1.30 % K^{-1} has been obtained in the I-BW for the sample Yb, Nd:Gd_2O_3, and for the II-BW, the maximum relative sensitivity was 0.82 % K^{-1} for the same sample. When working in the I-BW and II-BW, the thermal sensitivity of the Gd_2O_3 NPs is better that the KGW NPs. Thus, these luminescent nanoparticles seem to be good materials for nanothermometry and applications in the I-BW and II-BW.

5. ACKNOWLEDGEMENTS

Thanks to FiCNA - FiCMA research group for supported and assisted this work.

6. BIBLIOGRAPHY

[1] Brites C., Lima P., Silva N., Millán A., Amaral V., Palacio F. and Carlos, L., *Nanoscale,* 2012, **4**, 4799-4829.

[2] Rosal B., Pérez-Delgado A., Misiak M., Bednarkiewicz A., Vanetsev A., Orlovskii Y. and Jaque D., *J. Appl. Phys.* 2015, **118,** 143104.

[3] Benayas A. et al., *Adv. Optical. Mater,.* 2015, **3,** 687-694.

[4]Navarro E., Dirk H., Del Rosal B., Ren F., Benayas A., Vetrone F., Ma D., Sanz-Rodríguez F., García J., Jaque D. and Martín E., *Adv. Mater.* 2015, **27,** 4781-787.

[5] Wang Q., Qiu J., Song Z., Yang Z., Yin Z. and Zhou D. *Spectrochimica Acta Part A: Molecular and Biomolecular Spectroscop*y, 2015, **149**, 898-903.

[6] Jaque D. and Vetrone F., *Nanoscale,* 2012, **4**, 4301-4326.

[7] Savchuk, Ol. *Development of new materials and techniques for luminescence nanothermometry and photothermal conversion.* Thesis, Universitat Rovira i Virgili, Tarragona, 2016.

[8] Kai Y., Wan J., Zhang S., Tian B.., Zhang Y. and Liu Z., *Biomaterials,* 2012, **33**, 2206-214.

[9] Smith et al., *Nat. Nanotechnol.,* 2009, **4,** 710-711.

[10] Jiang G., Wei X., Zhou S., Chen Y., Duan X. and Yin M. , *J. Lumin.* 2014, **152**, 156-159.

[11] Roch U., Upendra K., Jacinto C., Villa I., Sanz-Rodríguez F., Iglesias M., Juarranz A., Carrasco E., Van Veggel F., Bovero E., García J. and Jaque D., *Small*, 2013, **10,** 1141-154.

[12] Wang D., Xue B., Kong X., Tu L., Liu X., Zhang Y., Chang Y., Luo Y., Zhao H. and Zhang H., *Nanoscale,* 2015, **7**, 190-197.

[13] Marciniak L. et al., *Phys. Chem.*, 2015, **17,** 24315-24321.

[14] Ximendes et al., *Nano Lett*., 2016, **16,** 1695.

[15] Savchuk Ol. et al., *J. Mater. Chem. C.*, 2016, **4**, 7397-405.

[16] Balabhadra S., Debasu M., Brites C., Nunes L., Malta O., Rocha J., Bettinelli M. and Carlos L., *Nanoscale*, 2015, **7,** 17261-7267.

[17] Pujol M. C. *Obtenció i caracterització de cristalls monoclínics de $KGd(WO_4)_2$ substituïts amb lantànids* Thesis, Universitat Rovira i Virgili, Tarragona, 2000.
[18] Pujol M. C. et al., *J. Appl Cryst*., 2011, **34,** 1-6.
[19] Zhaofeng W., Li Y., Jiang Q., Zeng H., Ci Z. and Sun L.., *J. Mater. Chem. C*., 2014, **22,** 4495.
[20] Kumar R., Prasad D., Shekher C., Prasad I. and Brahme N., *Indian Journal of Materials Science*, 2014, 1-7.
[21] Xiao H., Li P., Jia F. and Zhang L., *J. Phys. Chem. C*., 2009, **113,** 21034-1041.
[22] Galceran M. *Synthesis and characterization of optical nanocrystals and nanostructures. An approach to transparent laser nanoceramics*. Thesis, Universitat Rovira i Virgili, Tarragona, 2010.
[23] Barrera W. *Lanthanide-based dielectric nanoparticles for upconversion luminescence*. Thesis, Universitat Rovira i Virgili, Tarragona, 2013.
[24] Xiang S., Chen B., Zhang J., Li X., Sun J., Zheng H., Wu Z., Zhong H., Yu H. and Xia H., *Journal of Colloid and Interface Science*., 2014, **420,** 27-34.
[25] Yang X., Tang H. and Guo Z., *Superlattices and Microstructures,* 2015*,* **80,** 188-195.
[26] Monshi A. and Reza M., *World Journal of Nano Science and Engineering*, 2012, **2**, 154-160.
[27] Leroy A. and Klug H. *J. Appl. Phys.* 1950, **21,** 137-143.
[28] Inokuti M. and Hirayama F. *Phys. Chem.*, 1965, **43**, 6.
[29] Wade S. A., Collins S. F. and Baxter G. W., *J. Appl. Phys*., 2003, **94***,* 4743-4756.
[30] Orlovskii Y., Popov A., Platonov V., Fedorenko S., Sildos I. and Osipov V. *Journal of Luminescence,* 2013, **139,** 91-97.
[31] Bednarkiewicz A., Wawrzynczyk D., Nyk M. and Strek W., *Optical Materials,* 2011, **33,** 1481-486.
[32] Lupei A., Lupei V., Ikesue A. and Gheorghe C., *J. Opt. Soc. Am. B,* 2010, **27,** 1002.

Supplementary information

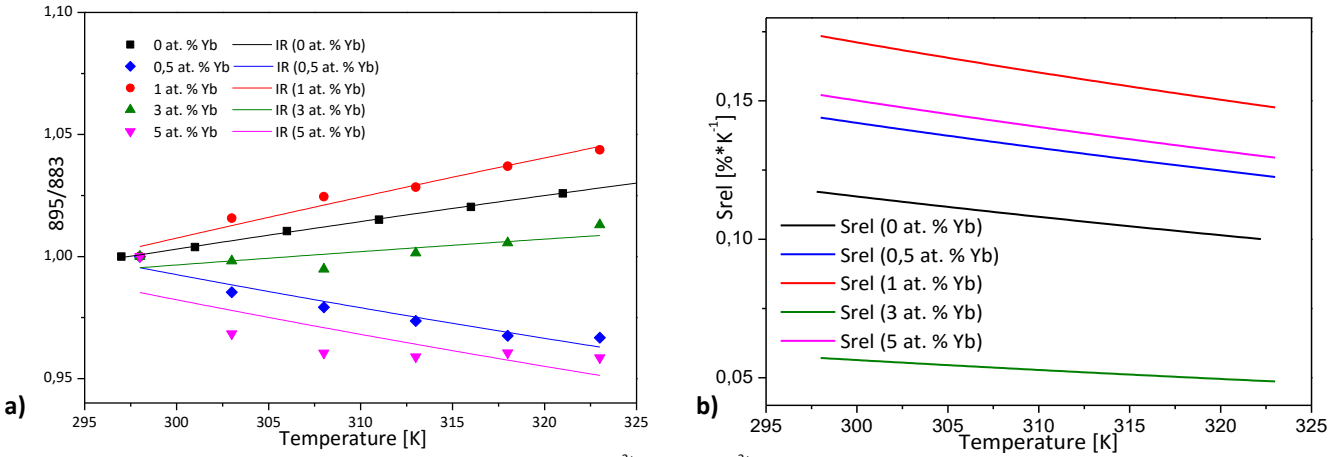

Figure 8: (a) Graphic of the intensity ratio (IR) I_{895}/I_{883} of the X at. % Yb^{3+}, 3 at. % Nd^{3+}: KGW NPs (X =0, 0.5, 1, 3 and 5). (b) Graphic of the relative selectivity (S_{rel}) of the x at. % Yb^{3+}, 3 at. % Nd^{3+}: KGW NPs (X =0, 0.5, 1, 3 and 5).

Table 3: S_{rel} of x at. % Yb, 3 at. % Nd:KGW NPs (x=0, 0.5, 1, 3 and 5) from 298 to 323K. The * is for the samples prepared by microwave-assisted hydrothermal.

x at. % Yb^{3+}	y at. % Nd^{3+}	Ratios	Transitions	S_{rel} [%*K^{-1}]
0.5	3	I_{873}/I_{899} (Nd^{3+})	$^4F_{3/2}$ (2') →$^4I_{9/2}$ (0) / $^4F_{3/2}$ (2') → $^4I_{9/2}$ (3)	0.54-0.46
		I_{873}/I_{1021} (Nd^3-Yb^{3+})	$^4F_{3/2}$ (2') →$^4I_{9/2}$ (0) / $^4F_{5/2}$ (0') →$^2F_{7/2}$ (2)	0.40-0.34
		I_{873}/I_{1094} (Nd^{3+} -Nd^{3+})	$^4F_{3/2}$ (2') →$^4I_{9/2}$ (0) / $^4F_{3/2}$ (1') →$^4I_{11/2}$ (5)	0.54-0.46
0	3	I_{895}/I_{883} (Nd^{3+})	$^4F_{3/2}$ (1') →$^4I_{9/2}$ (2) / $^4F_{3/2}$ (1') → $^4I_{9/2}$ (0)	0.12-0.10
0.5	3			0.14-0.12
1	3			0.17-0.15
3	3			0.06-0.05
5	3			0.15-0.13
0.5*	3*	I_{873}/I_{883} (Nd^{3+})	$^4F_{3/2}$ (2') →$^4I_{9/2}$ (0) / $^4F_{3/2}$ (1') → $^4I_{9/2}$ (0)	0.25-0.21
		I_{1060}/I_{1094} (Nd^{3+})	$^4F_{3/2}$ (2') →$^4I_{11/2}$ (0) / $^4F_{3/2}$ (1') →$^4I_{11/2}$ (5)	0.37-0.32
		I_{999}/I_{1094} (Yb^{3+})	$^4F_{5/2}$ (0') →$^2F_{7/2}$ (1) / $^4F_{3/2}$ (1') →$^4I_{11/2}$ (5)	0.30-0.26

Table 4: S_{rel} of 0.5 at. % Nd:Gd$_2$O$_3$ NPs and 0.5 at. % Yb, 3 at.% Nd:Gd$_2$O$_3$ NPs from 298 to 323K.

Gd_2O_3 NPs	Ratios	Transitions	S_{rel} [%*K^{-1}]
0.5 at.% Nd^{3+}	I_{879}/I_{942} (Nd^{3+})	$^4F_{3/2}$ (2')→ $^4I_{9/2}$ (1) / $^4F_{3/2}$ (1')→ $^4I_{9/2}$ (4)	0.33-0.28
	I_{1066}/I_{1073} (Nd^{3+})	$^4F_{3/2}$ (?') → $^4I_{11/2}$ (?) / $^4F_{3/2}$ (1') → $^4I_{11/2}$ (1)	0.46-0.39
	I_{879}/I_{1073} (Nd^{3+} -Nd^{3+})	$^4F_{3/2}$ (2')→ $^4I_{9/2}$ (1) / $^4F_{3/2}$ (1') → $^4I_{11/2}$ (1)	0.43-0.37
0.5 at.% Yb^{3+}, 3 at.% Nd^{3+}	I_{879}/I_{977} (Nd^{3+}-Yb^{3+})	$^4F_{3/2}$ (2')→ $^4I_{9/2}$ (1) / $^4F_{5/2}$ (0') →$^2F_{7/2}$ (0)	1.30-1.11
	I_{977}/I_{1052} (Yb^{3+}-Nd^{3+})	$^4F_{5/2}$ (0') →$^2F_{7/2}$ (0) / $^4F_{3/2}$ (2') → $^4I_{11/2}$ (0)	0.77-0.66
	I_{879}/I_{1099} (Nd^{3+}-Nd^{3+})	$^4F_{3/2}$ (2')→ $^4I_{9/2}$ (1) / $^4F_{3/2}$ (1') → $^4I_{11/2}$ (2)	0.82-0.70